Article | Open Access

Energy Materials

Li *et al*. *Energy Mater.* **2026**, *6*, 600049 **DOI:**10.20517/energymater.2025.227

$FeNiS_2$ quantum dot integration boosts enhanced reaction kinetics and cycle stability of SPAN nanofiber cathode for Li-S batteries

Jiajin Li[1], Ruoxi Niu[1], Haoyu Qi[1], Jinze Song[1], Yunling Wu[1,*], Lili Liu[1], Guoxing Li[1], Lijun Fu[1,*], Yuping Wu[1,2]

Keywords:
Lithium-sulfur batteries, $FeNiS_2$ quantum dots, catalytic conversion, reaction kinetics, high-rate performance

Citation: Li, J.; Niu, R.; Qi, H.; Song, J.; Wu, Y.; Liu, L.; Li, G.; Fu, L.; Wu, Y. $FeNiS_2$ quantum dot integration boosts enhanced reaction kinetics and cycle stability of SPAN nanofiber cathode for Li-S batteries. *Energy Mater.* **2026**, *6*, 600049. https://dx.doi.org/10.20517/energymater.2025.227

Received: 25 Dec 2025 **First Decision:** 16 Jan 2026 **Revised:** 5 Feb 2026 **Accepted:** 19 Mar 2026 **Published:** 12 May 2026

Academic Editor: Wei Tang
Copy Editor: Ping Zhang
Production Editor: Ping Zhang

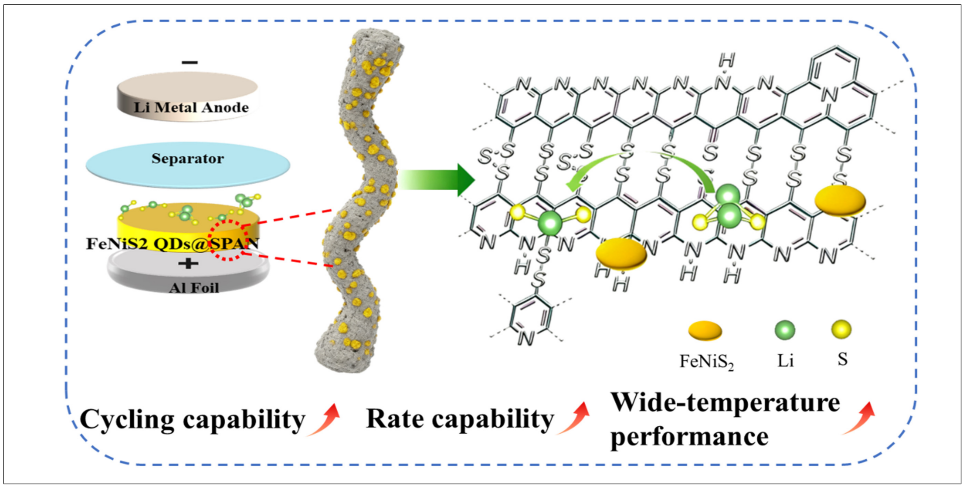

Abstract

Sulfurized polyacrylonitrile (SPAN) has been regarded as one of the most competitive cathode candidates for lithium-sulfur (Li-S) batteries, owing to its outstanding theoretical energy density, excellent structural durability, and minor self-discharge. Nevertheless, the intrinsically slow reaction kinetics of SPAN results in insufficient active sulfur utilization at high current rates, which severely restricts its rate performance and long-cycle stability. This study introduces $FeNiS_2$ Quantum Dots (QDs) as catalyst embedding in SPAN nanofibers ($FeNiS_2$ QDs@SPAN). Taking advantages of the ultra-small size, superior dispersibility and abundant catalytic sites of $FeNiS_2$ QDs, the redox kinetics and cycle performance of SPAN are significantly enhanced. Kinetic analyses and theoretical calculation demonstrate the uniformly dispersed $FeNiS_2$ QDs effectively reduce charge transfer resistance and facilitate conversion reaction. $FeNiS_2$ QDs@SPAN material exhibits high reversible capacity of 1,213 mAh g^{-1} and an ultralow capacity decay of 0.034% per cycle over 1,000 cycles at 1 C. Remarkably, even at high rate of 5 C (8.37 A g^{-1}), it delivers a stable long-cycle capacity of 720 mAh g^{-1} and demonstrates excellent cycling capability

[1]School of Chemistry and Molecular Engineering, State Key Laboratory of Materials-Oriented Chemical Engineering, and College of Energy Science and Engineering, Nanjing Tech University, Nanjing 211816, Jiangsu, China.
[2]School of Energy and Environment, Southeast University, Nanjing 211189, Jiangsu, China.

[*]**Correspondence to:** Assoc. Prof. Yunling Wu, Prof. Lijun Fu, School of Chemistry and Molecular Engineering, State Key Laboratory of Materials-Oriented Chemical Engineering, and College of Energy Science and Engineering, Nanjing Tech University, Nanjing 211816, Jiangsu, China. E-mail: ylwu@njtech.edu.cn; l.fu@njtech.edu.cn

with a low fade rate of 0.029% per cycle over 450 cycles. $FeNiS_2$ QDs@SPAN material maintains good performance even under lean electrolyte conditions and a wide temperature range. This work underscores the significant potential of $FeNiS_2$ QDs as catalyst for achieving high performance sulfur cathode and advanced Li-S batteries.

INTRODUCTION

Li-S batteries have emerged as a highly competitive electrochemical energy storage technology, mainly owing to their remarkable energy density (2,600 Wh kg^{-1}) and the low cost of their raw materials[1-3]. However, the widespread commercialization of Li-S batteries is still hindered by several intrinsic drawbacks. The sulfur itself is electronically insulated, and the reaction between sulfur and lithium sulfide (Li_2S) is sluggish. Particularly, the intermediate product lithium polysulfides (LiPSs) dissolve and diffuse in the ether electrolyte, and sulfur electrode suffers from severe shuttle effect, which leads to suboptimal utilization of active materials, poor cycle stability and even battery failure of the Li-S batteries[4-7]. Current research endeavors are aiming to mitigate the aforementioned concerns. Strategies such as physical confinement[8-10] and chemical absorption[11,12] of sulfur were used to suppress the shuttle effect. By introducing heterogeneous catalyst into the sulfur cathode, the redox reaction kinetics are accelerated[13,14]. Nevertheless, the unavoidable dissolution of long-chain LiPSs in ether-based electrolytes remains a critical issue.

As a sulfur-based cathode material, sulfurized polyacrylonitrile (SPAN) represents a promising candidate for Li-S batteries, which can be readily fabricated via heat treatment of polyacrylonitrile (PAN) under sulfur vapor[15,16]. Different from conventional sulfur-carbon composites prepared by physical blending, sulfur species in SPAN are covalently bonded to the conductive framework generated from PAN pyrolysis[17,18]. Although the precise molecular structure of SPAN has not been fully elucidated, it is widely accepted that sulfur is anchored onto the PAN-derived carbon support through covalent linkages. Accordingly, only short-chain LiPSs (Li_2S_n, $n \leq 4$) are involved in the electrochemical redox reactions upon cycling[19,20]. Thus, the notorious dissolution of LiPSs into electrolyte and shuttle effect of the sulfur cathode can be avoided. However, the slow kinetics of the solid-solid conversion reaction of SPAN would deteriorate the utilization of the sulfur and result in capacity fading of SPAN while cycling. In addition, the rate performance and cycle performance of the SPAN electrode under high rates are impacted as well[21]. To address the issue, electrocatalysts were explored and integrated into SPAN, which effectively anchors polysulfides and significantly improves the redox kinetics of SPAN electrode[22-24].

To optimize the cathode performance of Li-SPAN batteries, various catalytic materials have been developed to enhance the redox kinetics, including transition metal carbides, transition metal oxides, and transition metal sulfides. Among these candidates, transition metal sulfides presents combined merits, such as relatively higher electronic conductivity and good polar affinity for sulfur species, thus enabling dual functions of anchoring short-chain Li_2S_n and catalyzing their solid-solid conversion reactions during the operation of Li-S batteries[25-28]. For instance, Li *et al.*[29] incorporated cobalt sulfide (CoS_2) into SPAN, which enhanced its reactive activity and cycling stability, allowing the material to sustain over 500 cycles at 1 C. Liu *et al.*[30] synthesized NiS_2-SPAN powders using a simple co-heating method, which exhibited superior rate capabilities with a NiS_2 content of less than 3 wt%. Although transition metal sulfides are the most widely investigated category of metal sulfides for SPAN cathode modification, binary transition metal sulfides exhibit more abundant electrochemical active sites and more reactive polar surfaces compared with single transition metal sulfides[31,32]. This enables stable, rapid charge transport and sustained catalytic effects through multicomponent synergy and regulation of electronic band structures, which would boost the reaction kinetics[33,34]. Furthermore, to maximize the adsorption sites and catalytic efficiency for LiPSs, quantum dots (QDs), characterized by ultra-small size and superior dispensability, are particularly effective[35]. These QDs would significantly enhance the host-guest interactions, lower the reaction energy

barrier, and provide exceptional catalytic effects on LiPSs[36,37]. Yet, the application of binary-TMS (transition metal sulfides)-based QDs to modify SPAN for boosting the electrochemical properties of Li-SPAN batteries remains rarely reported.

In this study, we developed a novel $FeNiS_2$ QDs@SPAN composite by blending PAN/$NiFe_2O_4$ QDs nanofibers incorporated with sulfur powder, followed by a heat treatment. This process initiates polymerization and dehydrogenation reactions between PAN and sulfur, leading to the formation of pyridine ring structures. In the meantime, the $NiFe_2O_4$ QDs is sulfurized as $FeNiS_2$. The uniform dispersion of $FeNiS_2$ QDs throughout the composite increases the number of active sites, which enhances the charge transfer and accelerates the conversion of short-chain polysulfides. These improvements are crucial for optimizing the redox reaction kinetics. Meanwhile, the one-dimensional (1D) nanofibers maintain the structural integrity of the composite and provide short-distance diffusion pathways for ions. Benefiting from these synergistic advantages, the $FeNiS_2$ QDs@SPAN nanofibers exhibit excellent cycling stability and rate performance. Notably, the $FeNiS_2$ QDs@SPAN electrode achieves superior electrochemical performance at high rates, which is rarely reported for SPAN-based electrodes. It also maintains outstanding performance metrics across a wide temperature range and under lean electrolyte conditions, demonstrating great potential for practical application.

EXPERIMENTAL

Materials and methods

Preparation of $NiFe_2O_4$ QDs

All chemicals were of analytical grade or higher and used without further purification. [$Fe(NO_3)_3{\cdot}9H_2O$, > 99%], [$Ni(NO_3)_2{\cdot}6H_2O$, > 99%], PAN, N,N-dimethylformamide (DMF, ≥ 99.8%), concentrated ammonia (28%-30% NH_3), and Sublimed sulfur (99%) were all purchased from Sigma-Aldrich.

Approximately 10 mM of $Fe(NO_3)_3{\cdot}9H_2O$ and 5 mM of $Ni(NO_3)_2{\cdot}6H_2O$ were dissolved in 80 mL of deionized water. This solution was ultrasonicated for 30 min. Under ambient conditions, concentrated ammonia was added dropwise during magnetic stirring until the pH reached 8[35]. After an additional 10 min of stirring, the mixture was transferred to a Polytetrafluoroethylene (PTFE)-lined autoclave and heated at 190 °C for 8 h. Once cooled to room temperature, the upper layer of the resultant brown transparent liquid was collected via centrifugation and freeze-dried for later use.

Synthesis of PAN/$NiFe_2O_4$ QDs nanofibers

A mixture of 50 mg of $NiFe_2O_4$ QDs and 1 g of PAN was dispersed in 8.5 g of DMF and ultrasonicated for 2 h to ensure uniform dissolution and dispersion. The homogenized solution was then loaded into a 10 mL syringe and electrospun at a working voltage of 16 kV, a flow rate of 1 mL/h, with a 15 cm distance between the collector and the needle tip. The collector rotated at 100 rpm. A control sample of PAN without $NiFe_2O_4$ QDs was also prepared for comparison.

Synthesis of $FeNiS_2$ QDs@SPAN composites

Sublimed sulfur and PAN/$NiFe_2O_4$ QDs nanofibers were placed into a Flange high-pressure reaction tank. The mixture was heated under an argon atmosphere at 155 °C for 1 h, 350 °C for 2 h, and 450 °C for 5 h. To remove any excess sulfur, the sample was further heated at 200 °C for 2 h. A control sample without $NiFe_2O_4$ QDs, referred to as SPAN, was prepared under identical conditions for comparative purposes.

Material characterization

Elemental analysis (EA) was performed using an Elementar Vario EL analyzer (Elementar, Germany). Morphological characterization was carried out using a Carl Zeiss Supra 55 field-emission scanning electron microscope (SEM) equipped with an energy-dispersive X-ray spectroscopy (EDS) detector (Carl Zeiss, Germany). X-ray diffraction (XRD) patterns were recorded on a Rigaku SmartLab diffractometer with Cu-Kα radiation (Rigaku, Japan). Raman spectra were collected using a HORIBA LabRAM HR Evolution confocal Raman microscope (HORIBA Scientific, France).

Electrochemical measurement

The working cathode slurry was formulated by uniformly blending the $FeNiS_2$ QDs@SPAN composite with acetylene black and LA133 binder in a weight ratio of 80:10:10 in deionized water. This slurry was cast onto aluminum foil and dried under vacuum at 60 °C for 24 h. The dried electrode films were punched into discs with a diameter of 10 mm. The loading of $FeNiS_2$ QDs@SPAN on each electrode was approximately 1 mg cm^{-2} to 1.5 mg cm^{-2}. These 2025 coin cells were assembled in an argon-filled glove box using lithium metal as the anode. The electrolyte consisted of 1 M LiTFSI in a 1,3-Dioxolane (DOL)/DME (1:1 vol%) mixture with 2 wt% $LiNO_3$ added, with each cell containing approximately 60 μL of electrolyte (employed for all tests at both 0 °C and 60 °C). The charge/discharge performance was tested between 1 and 3 V at room temperature using a LAND CT 2001A multi-channel battery tester, with capacities calculated based on the mass of sulfur in the composite. Prior to high current density cycling, the assembled cells underwent pre-cycling activation at 0.1 C for 2 cycles. Cyclic voltammetry (CV) and electrochemical impedance spectroscopy (EIS) measurements were carried out on a CHI660 electrochemical workstation, with EIS frequencies ranging from 100,000 Hz to 0.01 Hz and an amplitude of 10 mV.

Theoretical calculations

Density Functional Theory (DFT) computations in this study were performed using the Vienna *Ab Initio* Simulation Package (VASP). Projector-augmented wave (PAW) potentials[38-40] and the Perdew-Burke-Ernzerhof (PBE) functional within the generalized gradient approximation (GGA)[41] were employed in the simulation. A 3 × 3 supercell of $FeNiS_2$ (102) surface was built. The vacuum space along the z-direction was set to 25 Å, while the plane-wave cutoff energy was set to 550 eV. The Brillouin zone of the supercell was sampled using a 2 × 2 × 1 *k*-point sampling grid, and the convergence tolerances for energy and force were set to 1.0 × 10^{-5} eV per atom and 10^{-2} eV $Å^{-1}$, respectively. Spin polarization was included to describe the ferromagnetic properties of $FeNiS_2$. The binding energy (E_b) of LiPSs on $FeNiS_2$ (102) surfaces was calculated using the following equation[13]:

$$E_b = E_{Sub+LiPS_S} - E_{LiPS_s} - E_{Sub}$$

where $E_{Sub+LiPS_S}$ is the total energy of the $FeNiS_2$ surface with adsorbed LiPSs, E_{LiPS_s} is the total energy of certain LiPSs, and E_{sub} is the total energy of $FeNiS_2$.

RESULTS AND DISCUSSION

Figure 1A and B illustrates the detailed procedure for synthesizing $FeNiS_2$ QDs@SPAN nanofibers. Initially, $NiFe_2O_4$ was synthesized using a hydrothermal method, and its aqueous dispersion exhibited bright blue luminescence under 365 nm Ultraviolet (UV) irradiation, confirming its quantum dot nature. A mixture of PAN and $NiFe_2O_4$ QDs was dispersed in DMF and stirred overnight to ensure solution homogeneity. This homogeneous solution was then loaded into a syringe for electrospinning, yielding $NiFe_2O_4$ QDs/PAN nanofiber precursors. Subsequently, these nanofibers were combined with sublimed sulfur in a high-pressure reaction vessel and subjected to heat treatment at 450 °C under an argon atmosphere. During this process, elemental sulfur (S_8) decomposed into smaller sulfur chains (-S_x-, where x < 8), facilitating the

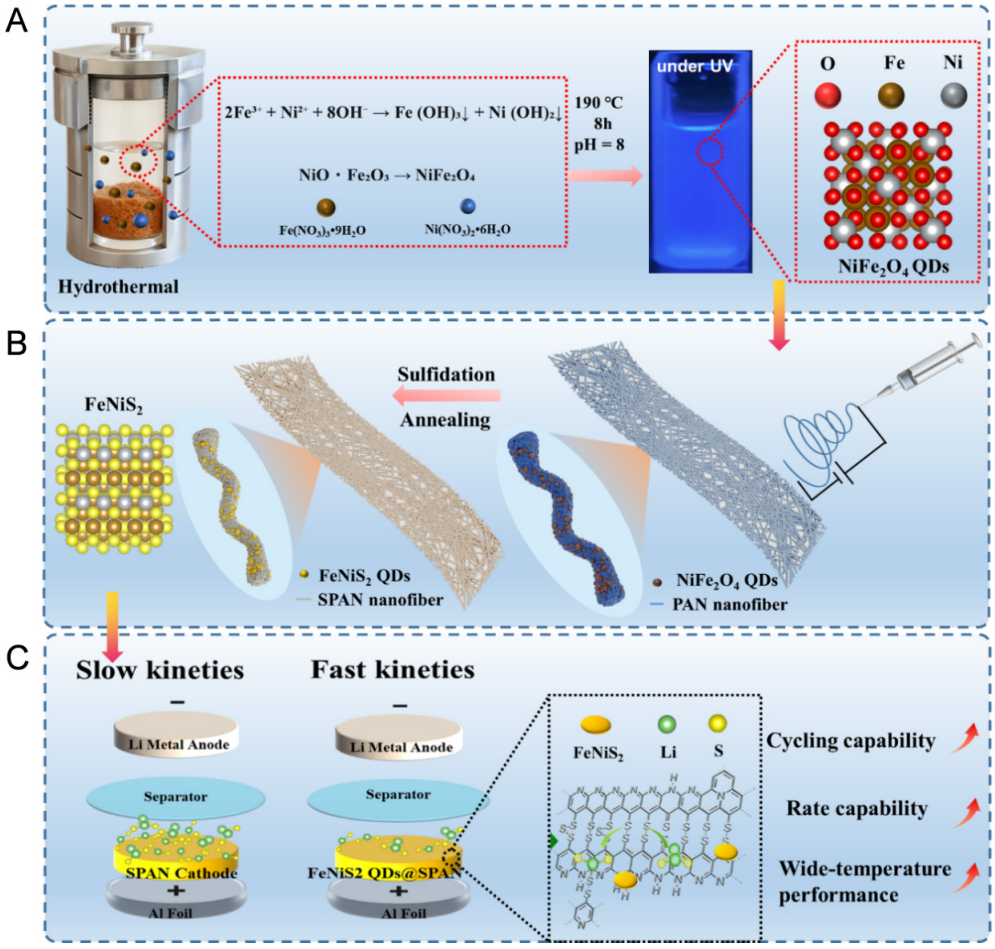

Figure 1. Schematic illustration for synthetic procedure of $FeNiS_2$ QDs@SPAN. QDs: Quantum dots; SPAN: sulfurized polyacrylonitrile; PAN: polyacrylonitrile; UV: ultraviolet.

dehydrogenation and cyclization of PAN. Finally, a further heating step at 200 °C in a quartz tube furnace under argon flow was employed to remove any adsorbed excess sulfur, resulting in the formation of $FeNiS_2$ QDs@SPAN which exhibited excellent kinetic performance as a cathode [Figure 1C].

SEM images of $NiFe_2O_4$ QDs@PAN and $FeNiS_2$ QDs@SPAN are depicted in Supplementary Figure 1 and Figure 2A, respectively. The $NiFe_2O_4$ QDs@PAN sample displays a nanofiber mesh structure, characterized by long, uniformly interconnected fibers possessing an average diameter of roughly 165 nm. For $FeNiS_2$ QDs@SPAN, the integrity of the nanofiber network remains intact throughout the vulcanization process, with no visible sulfur particles adhering to the fiber surfaces. In addition, the $FeNiS_2$ QDs@SPAN sample exhibits an increased fiber diameter of approximately 320 nm, and the nanofiber surface becomes rough, attributed to the infiltration of saturated sulfur species. A similar phenomenon can be observed in both PAN and SPAN, as shown in Supplementary Figure 2.

The High-Resolution Transmission Electron Microscopy (HR-TEM) images reveal the $FeNiS_2$ QDs@SPAN contains both crystalline and high-contrast disordered regions [Figure 2B and C]. A lattice spacing of 0.26 nm is clearly observed [Figure 2D], combined Fast Fourier Transform (FFT) analysis corroborates that the interplanar spacings that precisely match the (101) planes of the cubic phase $FeNiS_2$. Furthermore, EDS mapping in the TEM confirm the uniform distribution of Ni, Fe, and S within the nanofibers [Figure 2E-H], indicating the homogeneous dispersion of $FeNiS_2$ QDs within the SPAN matrix without significant

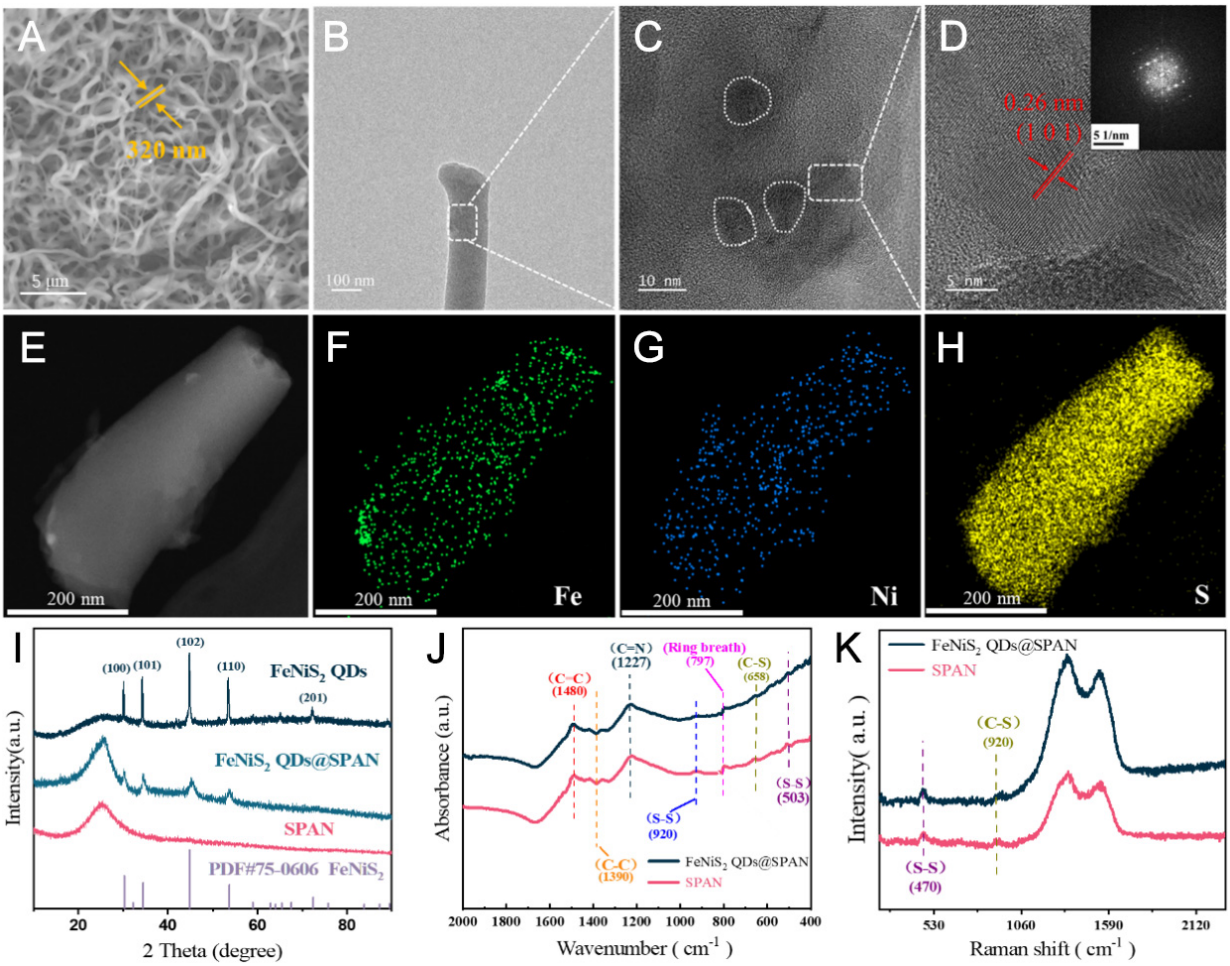

Figure 2. Characterization of $FeNiS_2$ QDs@SPAN and SPAN. SEM images of (A) $FeNiS_2$ QDs@SPAN, (B and C) HR-TEM image of $FeNiS_2$ QDs@SPAN with an inset in (D) showing the corresponding FFT pattern; (E-H) TEM images along with EDS elemental mapping of $FeNiS_2$ QDs@SPAN composite; (I) XRD patterns of SPAN and $FeNiS_2$ QDs@SPAN; (J) FT-IR and (K) Raman spectra of SPAN and $FeNiS_2$ QDs@SPAN, respectively. QDs: Quantum dots; SPAN: sulfurized polyacrylonitrile; EDS: energy-dispersive X-ray spectroscopy; XRD: X-ray diffraction; FT-IR: fourier transform infrared spectroscopy; HR-TEM: high-resolution transmission electron microscopy; FFT: fast fourier transform.

aggregation. And the $FeNiS_2$ content is 2.6 wt% according to the EDS analysis. The elemental composition of the $FeNiS_2$ QDs@SPAN and SPAN was quantitatively analyzed via ElementalAanalysis (EA), with the detailed results presented in Supplementary Table 1. The EA results indicate a sulfur content of 42% in SPAN and 46% in $FeNiS_2$ QDs@SPAN, demonstrating nearly identical levels of sulfur in both materials. The introduction of a trace amount of $FeNiS_2$ QDs did not impede the crosslinking process of PAN nanofibers with sulfur, thereby retaining a high sulfur content.

XRD measurements are performed to characterize the phase composition and crystalline properties of the resultant materials. The XRD patterns for various samples, including $NiFe_2O_4$ QDs, $FeNiS_2$ QDs, SPAN, and $FeNiS_2$ QDs@SPAN, are illustrated in Figure 2I and Supplementary Figure 3. The XRD spectra for $NiFe_2O_4$ QDs display characteristic peaks at 30.2°, 35.6°, 37.3°, 43.3°, 53.8°, 57.35°, and 62.92°, corresponding to the (220), (311), (222), (400), (442), (511), and (440) planes respectively, this aligns with the spinel structure of $NiFe_2O_4$ (PDF #054-0964)[42]. The XRD patterns for both $FeNiS_2$ QDs and $FeNiS_2$ QDs@SPAN closely match the standard phase of $FeNiS_2$ (PDF card No. 75-0606), with identifiable peaks at 30.25°, 34.4°, 44.8°, 53.8°, 65.4°, and 72.5°, corresponding to the (100), (101), (102), (110), (201), and (202)planes of

$FeNiS_2$[43]. For the $FeNiS_2$ QDs@SPAN composites, broad diffraction peaks observed between 20° to 30° predominantly result from the overlap of the characteristic graphene (002) peak with the amorphous peak of SPAN. The above characterization results collectively confirm that the $FeNiS_2$ QDs@SPAN composite has been successfully synthesized.

The Fourier Transform Infrared Spectroscopy (FT-IR) spectroscopic analysis of the as-prepared samples is presented in Figure 2J. Two distinct absorption peaks appearing at 503 and 920 cm^{-1} correspond to the stretching vibrations of disulfide (S-S) linkages, while the absorption signal at 658 cm^{-1} is derived from the stretching vibration of carbon-sulfur (C-S) bonds. Additionally, the characteristic peaks at 1,480 and 1,349 cm^{-1} belong to the typical vibrational modes of carbon-carbon double bonds (C=C) and single bonds (C-C), in sequence. A peak at 1,227 cm^{-1} is attributed to carbon-nitrogen (C=N) bond vibrations, indicating specific organic features. The 797 cm^{-1} peak suggests cyclic compounds in the material[44]. The FT-IR spectra of $FeNiS_2$ QDs@SPAN and SPAN are almost identical, indicating that the incorporation of $FeNiS_2$ QDs does not significantly alter the molecular structure of SPAN. The Raman spectroscopic analysis of $FeNiS_2$ QDs@SPAN and SPAN composites is illustrated in Figure 2K. The $FeNiS_2$ QDs@SPAN sample exhibits two dominant characteristic peaks at 1,340 and 1,558 cm^{-1}, corresponding to the D- and G-bands of carbon, respectively. In addition, a distinct absorption peak at 470 cm^{-1} is observed, which is assigned to the stretching mode of C-S bonds, verifying that sulfur has been chemically grafted onto the carbon matrix via covalent linkages during the thermal treatment process. The characteristic peak at 920 cm^{-1} is attributed to the stretching vibration of six-membered ring structures[45]. With I_G/I_D values below 1 for both composites, $FeNiS_2$ QDs@SPAN possesses a graphite-like stacked structure identical to that of pristine SPAN. These results confirm that PAN undergoes dehydrocyclization to form a six-membered aromatic framework with π-π stacking interactions, while sulfur species are anchored to the carbonaceous conductive matrix in the form of short-chain sulfur moieties. In summary, the incorporation of $FeNiS_2$ QDs exerts no discernible influence on the crosslinking reaction of PAN with sulfur.

To assess the impact of $FeNiS_2$ QDs on Li-S battery electrochemistry, corresponding cells were assembled with a metallic lithium anode and $FeNiS_2$ QDs@SPAN/SPAN cathodes for performance investigation. Rate capability is an important parameter for practical rechargeable battery systems. As illustrated in Figure 3A, the rate performance of two cathodes was evaluated by conducting charge/discharge cycles with varying rates from 0.5 C to 5 C. Both specific capacities and current rates are normalized with respect to the sulfur mass. The $FeNiS_2$ QDs@SPAN cathode delivers specific discharge capacities of 1,300, 1,180, 1,050, 1,005, and 880 mAh g^{-1} at 0.5, 1, 2, 3 and 4 C, respectively (1 C = 1,675 mAh g^{-1}). The $FeNiS_2$ QDs@SPAN cathode demonstrates a higher discharge capacity compared to the battery with SPAN cathode at all current densities. Even when cycled at an ultra-large current density of 5 C during rate testing, the $FeNiS_2$ QDs@SPAN cathode retains a specific discharge capacity as high as 761.2 mAh g^{-1}, which is remarkably superior to that of the pristine SPAN counterpart (438 mAh g^{-1}). Upon switching the current density back to 0.5 C, the $FeNiS_2$ QDs@SPAN cathode recovers a high reversible capacity of 1,209 mAh g^{-1}, verifying its outstanding reversibility and rate stability. Notably, the pure $FeNiS_2$ QDs electrode shows negligible capacity under identical experimental conditions, as illustrated in Supplementary Figure 4A and B. Furthermore, CV analysis reveals that the $FeNiS_2$ QDs electrode demonstrates very low peak currents, indicating that the quantum dots themselves contribute little to the electrochemical capacity.

The charge-discharge profiles of the $FeNiS_2$ QDs@SPAN cathode at various current densities are presented in Figure 3B. Apparently, even under an ultra-high rate of 5 C, all discharge curves show a stable and flat voltage platform. In contrast, it is clear that the SPAN cathode experiences severe capacity degradation and greater polarization as the current density increases [Supplementary Figure 5]. The potential difference (discharge mid-voltage minus charge mid-voltage equals ΔE) between the discharge and charge curves

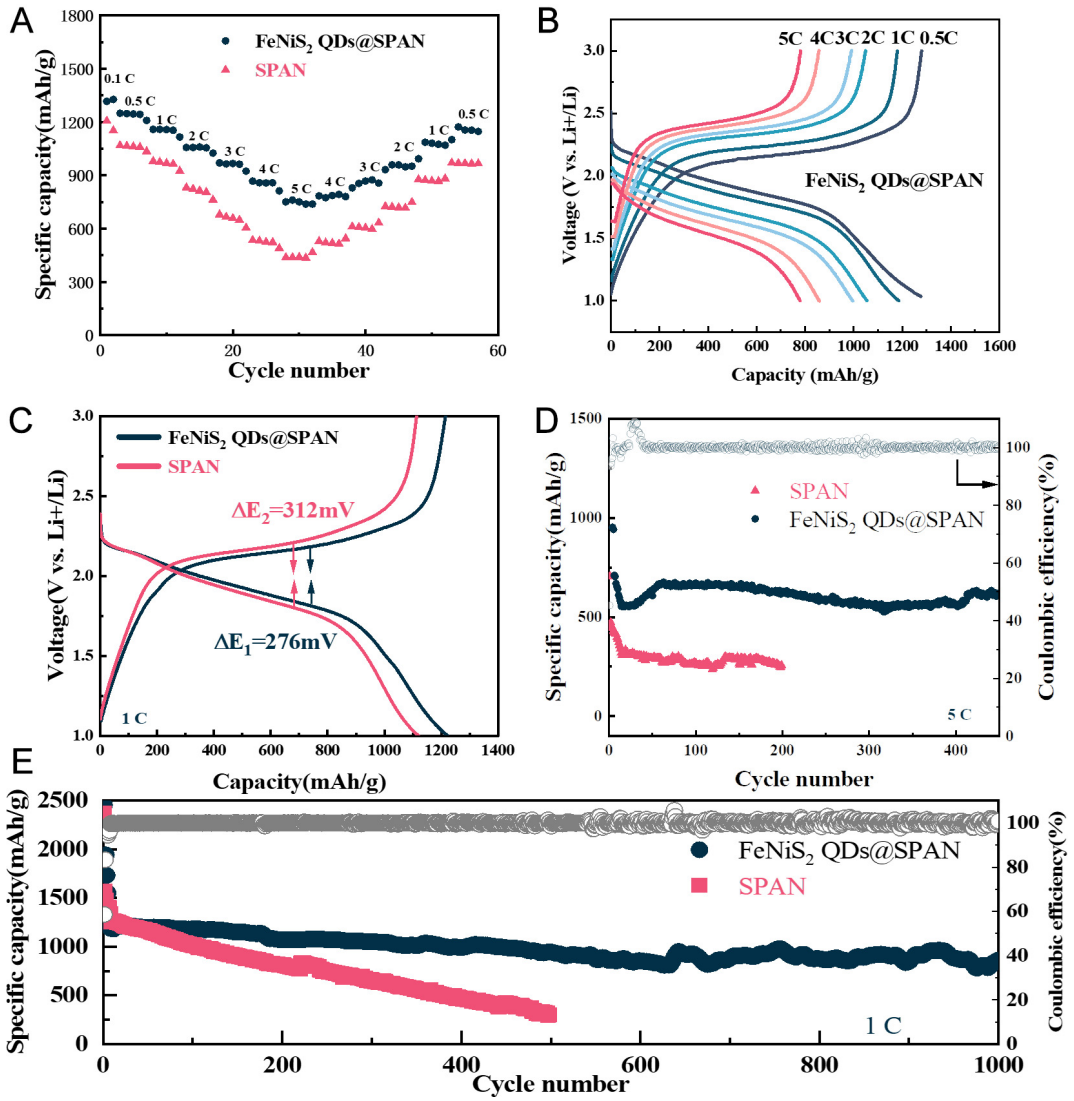

Figure 3. Electrochemical properties of $FeNiS_2$ QDs@SPAN cathode. (A) rate performance of both $FeNiS_2$ QDs@SPAN and SPAN cathodes; (B) charge/discharge profiles of the $FeNiS_2$ QDs@SPAN cathode across various current rates from 0.5 C to 5 C; (C) Galvanostatic charge-discharge profiles for both $FeNiS_2$ QDs@SPAN and SPAN cathodes at 1 C; (D) Cycling stability performance of both the $FeNiS_2$ QDs@SPAN and SPAN at 5 C; (E) Cyclic performance of the $FeNiS_2$ QDs@SPAN and SPAN cathode at 1 C. QDs: Quantum dots; SPAN: sulfurized polyacrylonitrile.

represents the degree of polarization. As shown in Figure 3c, compared to SPAN (ΔE_2 = 312 mV), the $FeNiS_2$ QDs@SPAN (ΔE_1 = 276 mV) cathode shows a smaller voltage hysteresis and a higher reversible capacity. This mainly benefits from the catalytic activity of $FeNiS_2$ QDs for the electrochemical redox reactions, which facilitates the kinetic properties.

To evaluate the long-term cycling performance of Li-S batteries under high current densities, both cathodes were cycled at a fixed current rate of 5 C [Figure 3D]. SPAN experiences a structural rearrangement during the first discharge process[46], therefore the SPAN and $FeNiS_2$ QDs@SPAN electrodes were activated at 0.1 C for 2 cycles to complete the structural reorganization. After activating the $FeNiS_2$ QDs@SPAN electrode, it exhibits a discharge specific capacity of 720 mAh g^{-1} when the current density is switched to 5 C (8.37 A g^{-1}). Impressively, after 450 cycles, the $FeNiS_2$ QDs@SPAN electrode maintains 86.6% capacity retention (624 mAh g^{-1}), corresponding to a low fade rate of 0.029% per cycle. For the SPAN electrode, the discharge

capacity is only 500 mAh g^{-1} when initially cycled at 5 C, and it can barely be cycled after 200 cycles. The superior performance of $FeNiS_2$ QDs@SPAN electrode highlights the role of $FeNiS_2$ QDs with enhanced adsorption and catalytic sites, which promotes the efficient conversion reaction between lithium polysulfides and Li_2S, and endows the high capacity as well as improved cycle stability over extended cycles.

The long-term cycling test results in Figure 3E reveal that the $FeNiS_2$ QDs@SPAN cathode delivers an initial specific discharge capacity as high as 1,210 mAh g^{-1} under 1 C, with an ultra-low average capacity decay rate of only 0.034% across 1,000 cycles. After 1,000 cycles, the Coulombic Efficiency (CE) of the $FeNiS_2$ QDs@SPAN cathode can still be stabilized at 99.3%. In contrast, the SPAN cathode initially shows a comparable discharge capacity to the $FeNiS_2$ QDs@SPAN cathode, and it suffers a drastic capacity drop with the capacity retention of only 24% after 500 cycles at 1 C. This suggests that the $FeNiS_2$ QDs show a pronounced effect in facilitating the thorough and rapid conversion of the sulfur redox reaction, which sustains the high utilization efficiency of the active materials. Supplementary Figure 6 shows the morphology of the $FeNiS_2$ QDs@SPAN cathode observed after 200 cycles at 1 C, demonstrating it still maintain its fiber structure after cycling. The above results indicate that $FeNiS_2$ QDs are crucial for enhancing the reaction kinetics, rate performance, and long-term cycling stability of the $FeNiS_2$ QDs@SPAN cathode. For comparison, we have collated the electrochemical performance metrics of SPAN-based cathode materials reported in prior works, as summarized in Supplementary Table 2[30,44,46-52]. It can be seen that the rate capacity and cyclic stability of the $FeNiS_2$ QDs@SPAN electrode are superior to those reported in the literature. Particularly, the $FeNiS_2$ QDs@SPAN cathode achieves 450 stable cycles at 5 C (8.37 A g^{-1}), a record cycle and rate performance for SPAN-based cathode, according to the authors' best knowledge[29,30,44,49,53-56].

To investigate the catalytic properties of the $FeNiS_2$ QDs@SPAN composite in lithium-sulfur reactions, the corresponding electrocatalytic performance was systematically investigated by combining CV with Tafel measurements. The typical CV curves of the two electrodes, obtained at a scan rate of 0.2 mV s^{-1}, are illustrated in Figure 4A. Two well-resolved broad cathodic peaks at 2.08 and 1.73 V can be clearly observed for the $FeNiS_2$ QDs@SPAN nanofiber electrode, originating from the stepwise electrochemical reduction of short-chain sulfur to Li_2S_2 and Li_2S, in sequence[29]. For SPAN, merely a single broad cathodic peak emerges at 1.62 V, a feature indicative of pronounced polarization along with a shift toward lower potentials. These results confirm that $FeNiS_2$ QDs can expedite the reduction reaction of SPAN and enhance the reaction kinetics during the discharging process. To better understand the catalytic activity of $FeNiS_2$ QDs, we compared the Tafel plots for a single cathodic and anodic process, respectively, as shown in Figure 4B and C. For the reduction process, the estimated Tafel slope for the $FeNiS_2$ QDs@SPAN cathode is 131.2 mV dec^{-1}, which is significantly smaller than that of the SPAN electrode (317.3 mV dec^{-1}). Similarly, for the oxidation process, the $FeNiS_2$ QDs@SPAN cathode exhibits a lower Tafel slope of 0.998 V dec^{-1} in comparison with the SPAN electrode (1.634 V dec^{-1}). This indicates that with the $FeNiS_2$ QDs, lower polarization and enhanced redox conversion between LiPS and Li_2S of the $FeNiS_2$ QDs@SPAN electrode can be realized, in comparison to the SPAN electrode.

To further understand the improved kinetics of $FeNiS_2$ QDs@SPAN, EIS measurements were conducted. The results demonstrate significantly enhanced charge transfer capability of the $FeNiS_2$ QDs@SPAN composite before and after cycling. Before cycling, the Nyquist plots [Figure 4D] exhibited characteristic impedance spectra, which comprise a distinct high-frequency semicircle attributed to the interfacial charge transfer resistance (R_{ct}), as well as a diagonal line at low frequency related to the Warburg impedance (W_o) of Li^+ diffusion in the electrode. Analysis of the fitting data shows that $FeNiS_2$ QDs@SPAN exhibits substantially lower R_{ct} (124.5 Ω) than the SPAN electrode (198.7 Ω) before cycling [Supplementary Table 3]. Furthermore, Figure 4E confirms that the R_{ct} of $FeNiS_2$ QDs@SPAN after cycling remains markedly lower than that of SPAN, which is attributable to the composite's superior catalytic properties in promoting Li_2S_2/Li_2S

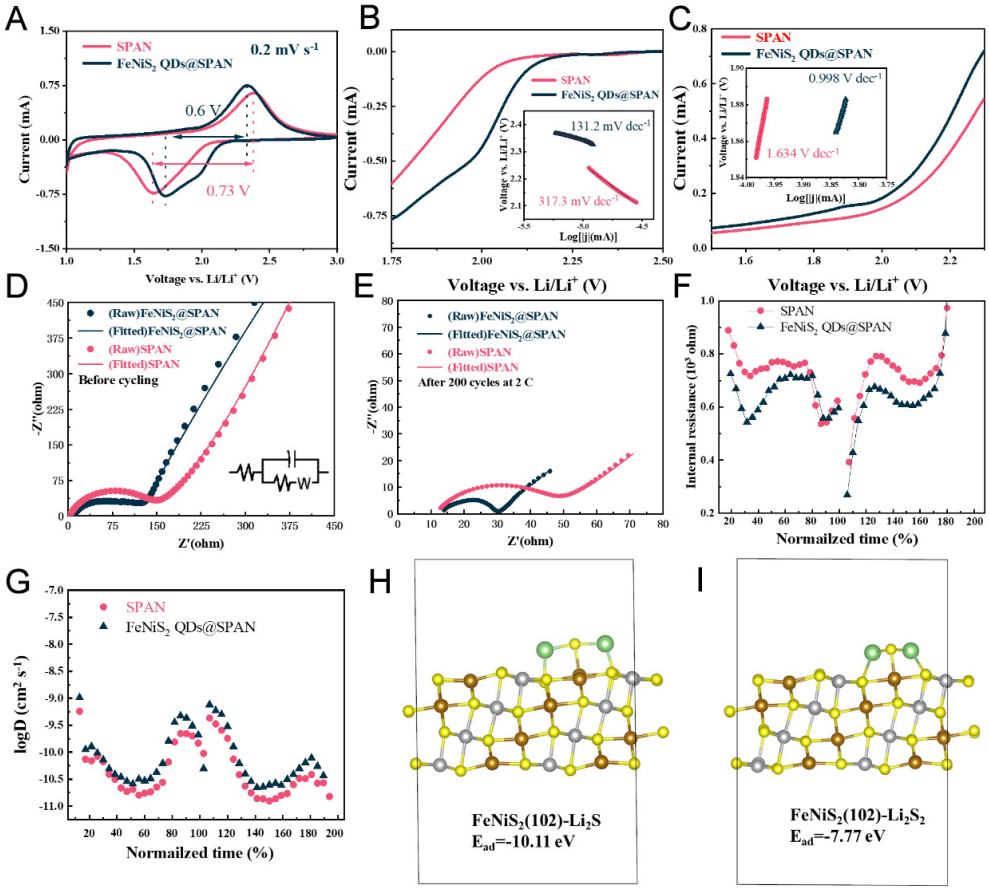

Figure 4. Reaction kinetics investigation of $FeNiS_2$ QDs@SPAN and SPAN electrodes. (A) The comparison of peak voltages for $FeNiS_2$ QDs@SPAN and SPAN electrodes from the CV curve; (B and C) Tafel plots of the cathodic reduction process, and the anodic oxidation process; Impedance spectroscopy of the (D and E) EIS spectra of $FeNiS_2$ QDs@SPAN and SPAN before and after 200 cycles at 2 C; (F) Internal resistances of the $FeNiS_2$ QDs@SPAN and SPAN electrode relative to the normalized discharge-charge time; (G) Li^+ diffusion coefficients calculated from GITT profiles according to overpotential; Adsorption configurations of (H) Li_2S and (I) Li_2S_2 on the $FeNiS_2$ (102) surface. QDs: Quantum dots; SPAN: sulfurized polyacrylonitrile; EIS: electrochemical impedance spectroscopy; GITT: galvanostatic intermittent titration technique.

conversion kinetics [Supplementary Table 3]. Additionally, Variable-scan-rate CV (0.2-1 mV s^{-1}) and Galvanostatic Intermittent Titration Technique (GITT) investigation further confirm the fast reaction kinetics of $FeNiS_2$ QDs@SPAN, as manifested by enhanced Li diffusion coefficient obtained via the two methods (details see Figure 4F and G, Supplementary Figures 7 and 8).

The adsorption behavior of Li_2S_n (n = 1, 2) on $FeNiS_2$ was further investigated by DFT calculations. The (102) crystal plane is selected for the DFT calculation since the XRD pattern of the synthesized $FeNiS_2$ shows that (102) is the strongest peak [Figure 2I]. Figure 4H and I, Supplementary Figure 9 illustrate the optimized adsorption configurations and the corresponding top views of Li_2S and Li_2S_2 on the $FeNiS_2$ (102) surface, respectively. The adsorption energies of Li_2S_2 and Li_2S on the $FeNiS_2$ (102) surface are computed to be -7.77 and -10.11 eV, respectively. These values are significantly more negative than those on pyridine nitrogen sites (in N-doped carbon)[57,58], demonstrating that the introduction of $FeNiS_2$ provides much stronger anchoring for Li_2S_2 and Li_2S. It might lead to the formation of Li_2S_2 and Li_2S close to the homogeneously dispersed $FeNiS_2$ during the reduction reaction, which further facilitates the conversion reaction between LiPS and Li_2S_2/Li_2S.

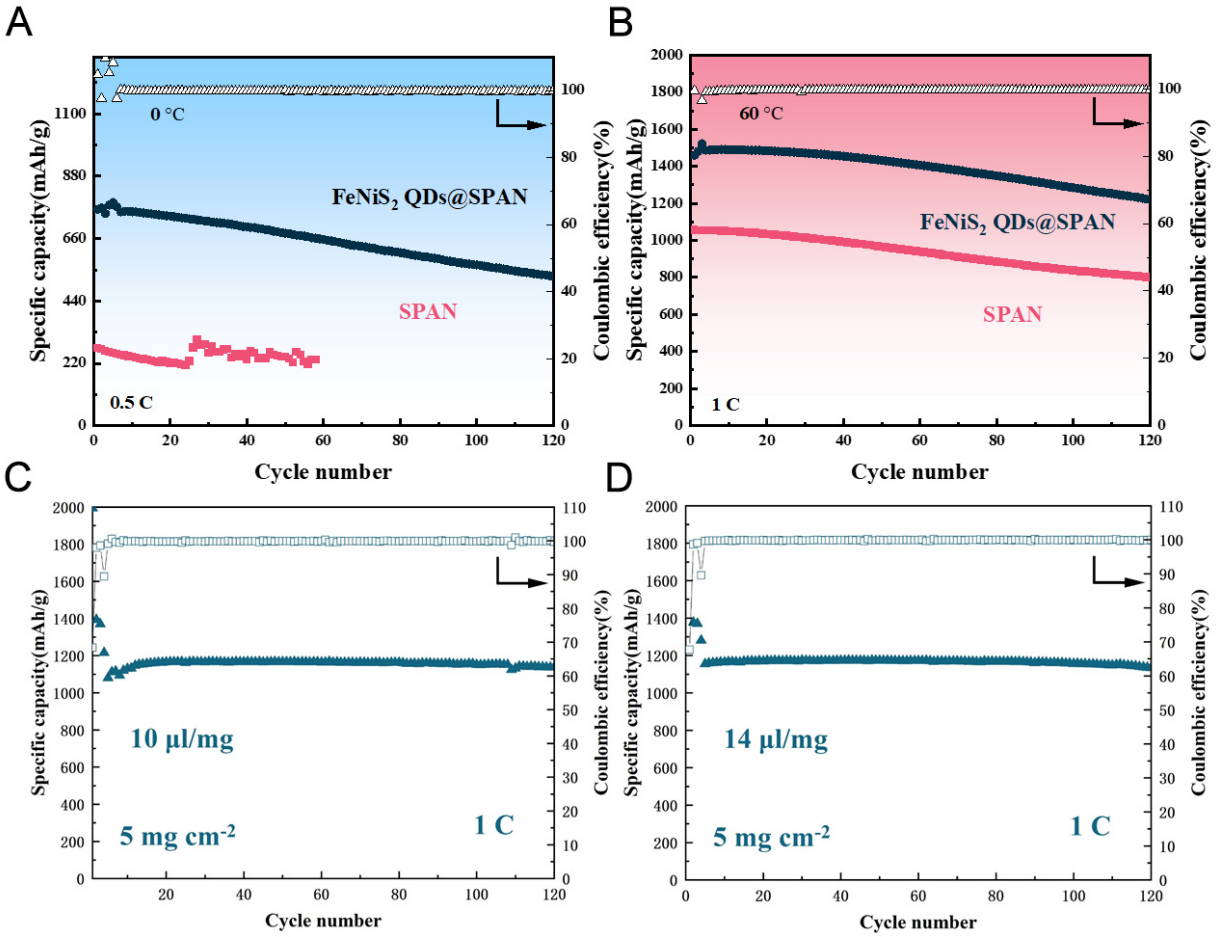

Figure 5. Electrochemical cycling performance of the $FeNiS_2$ QDs@SPAN composite under different temperatures and conditions. (A) Cycling performance of $FeNiS_2$ QDs@SPAN and SPAN electrodes at 0.5 C and 0 °C; (B) Corresponding performance at 1 C and 60 °C; (C and D) E/S ratio effects on $FeNiS_2$ QDs@SPAN cycling at 1 C with ratios of 10 and 14 µL mg^{-1}. QDs: Quantum dots; SPAN: sulfurized polyacrylonitrile; E/S: electrolyte-to-sulfur.

To investigate the feasibility of $FeNiS_2$ QDs@SPAN for extreme environmental conditions, the performance of SPAN electrodes across a broad temperature range was further evaluated.As shown in Figure 5A and Supplementary Figure 10A, the $FeNiS_2$ QDs@SPAN cathode delivered a remarkable specific discharge capacity of 751 mAh g^{-1} at 0.5 C under 0 °C. Despite the increased electrolyte viscosity and sluggish reaction kinetics at 0 °C, the $FeNiS_2$ QDs@SPAN cathode still maintained 71% of its initial capacity after 120 cycles. This outstanding cycle stability of $FeNiS_2$ QDs@SPAN cathode at 0 °C arises from the high electrocatalytic activity of $FeNiS_2$ QDs, which effectively promotes polysulfide conversion and enhances the reaction kinetics. In stark contrast, SPAN electrode shows an initial capacity of merely 440 mAh/g at 0 °C. It suffers rapid capacity decay and short-circuit after only 60 cycles, demonstrating very poor low-temperature tolerance. The high-temperature cycling performance at 60 °C is presented in Figure 5B and Supplementary Figure 10B. After two activation cycles at 0.1 C, the $FeNiS_2$ QDs@SPAN composite cathode achieved an impressive specific discharge capacity of 1,487 mAh g^{-1} at a current rate of 1 C, and retained a capacity retention of 83% after 120 cycles. By comparison, the SPAN cathode only delivered a much lower specific capacity of 1,054 mAh g^{-1} at 1 C and 60 °C. The results highlight that the effects of $FeNiS_2$ QDs on boosting the reaction kinetics and overall electrochemical performance of the SPAN cathode in the temperature range of 0 and 60 °C.

To demonstrate the commercial viability of $FeNiS_2$ QDs@SPAN material, its performance was tested under high sulfur loading and lean electrolyte environments. Coin cells with 5 mg cm^{-2} $FeNiS_2$ QDs@SPAN electrode and different electrolyte-to-sulfur (E/S) ratios of 7, 10, 14, and 18 μL mg^{-1} were assembled and their performance was evaluated. All cells exhibit similar galvanostatic charge-discharge profiles, and maintain the characteristic SPAN charge-discharge curves [Supplementary Figure 11]. With a lower E/S ratio of 7 μL mg^{-1}, the polarization is slightly increased. Cycle stability under varied E/S ratios was further investigated. As shown in Figure 5C and D, Supplementary Figure 12, the initial specific capacities of $FeNiS_2$ QDs@SPAN in all cells are almost same, which confirms the sulfur utilization is unaffected with different E/S ratios. Specifically, the capacities of $FeNiS_2$ QDs@SPAN in the cells with E/S ratios of 7, 10, 14, and 18 μL mg^{-1} are 1,173, 1,159, 1,174, and 1,169 mAh g^{-1}, respectively. For the cells with E/S ratios of 10, 14, 18 μL mg^{-1}, they show excellent cycle stability, and the capacity retention is 97.9%, 96.1%, and 98.7% over 120 cycles, respectively. When tested at a lean electrolyte condition with an E/S ratio as low as 7 μL mg^{-1}, the cell exhibited a gradual capacity decay, and retained 70.6% of its initial capacity after 100 cycles. This performance degradation is mainly ascribed to the increased voltage polarization, as illustrated in Supplementary Figure 10.The results suggest that $FeNiS_2$ QDs@SPAN electrode with 5 mg cm^{-2} mass loading exhibits excellent cycling performance when the E/S ratio is above 10 μL mg^{-1}. It demonstrates promising application potential of $FeNiS_2$ QDs@SPAN material for lithium sulfur batteries.

CONCLUSIONS

In summary, this work aims to address the intrinsically slow reaction kinetics of SPAN cathodes for Li-S batteries by fabricating $FeNiS_2$ QDs@SPAN nanofibers via electrospinning coupled with sulfurization heat treatment. The embedded $FeNiS_2$ QDs act as efficient catalytic sites, which reduce the cathode charge transfer resistance and accelerate the conversion of short-chain polysulfides to Li_2S, thereby effectively boosting the intrinsic reaction kinetics of SPAN. This catalytic modification endows the $FeNiS_2$ QDs@SPAN cathode with excellent rate performance, cycling stability, and reliable electrochemical performance under harsh working conditions including a wide temperature range and lean electrolyte. Further optimization of electrode structure may enhance the performance of Li//$FeNiS_2$ QDs@SPAN battery under even leaner electrolyte conditions. This study verifies that integrating $FeNiS_2$ QDs catalysts into SPAN nanofibers is a feasible and effective strategy for advancing SPAN-based Li-S batteries, and it provides a valuable reference for the design of high-performance catalytic electrodes for high-energy-density Li-S batteries.

DECLARATIONS

Authors' contributions

Methodology, software, investigation, writing original draft: Li, J.
Validation, formal analysis, visualization: Niu, R.
Writing-review and editing: Qi, H.; Song, J.
Writing-reviewing, discussion: Wu, Y. (Yunling Wu); Liu, L.; Li, G.
Conceptualization, writing-review and editing, supervision, data curation, project administration: Fu, L.
Writing-reviewing, discussion, resources: Wu, Y. (Yuping Wu)

Availability of data and materials

The data that support the findings of this study are available from the corresponding author upon reasonable request.

AI and AI-assisted tools statement

Not applicable.

Financial support and sponsorship

This work was supported by the National Natural Science Foundation of China (52122209, 52373289, 52403001).

Conflicts of interest

Yuping Wu serves as the Editor-in-Chief of the journal *Energy Materials*; however, he was not involved in any stage of the editorial process for this manuscript, including reviewer selection, manuscript handling, or decision-making. The other authors declare that they have no conflicts of interest.

Ethical approval and consent to participate

Not applicable.

Consent for publication

Not applicable.

Copyright

Supplementary Materials

Supplementary Materials

REFERENCES

1. Fang, R.; Zhao, S.; Sun, Z.; Wang, D. W.; Cheng, H. M.; Li, F. More reliable lithium-sulfur batteries: status, solutions and prospects. *Adv. Mater.* **2017**, *29*, 1606823. DOI
2. Deng, R.; Wang, M.; Yu, H.; et al. Recent advances and applications toward emerging lithium-sulfur batteries: working principles and opportunities. *Energy. Environ. Materials.* **2022**, *5*, 777-99. DOI
3. Wang, J.; He, Y. S.; Yang, J. Sulfur-based composite cathode materials for high-energy rechargeable lithium batteries. *Adv. Mater.* **2015**, *27*, 569-75. DOI
4. Sun, C.; Sheng, J.; Zhang, Q.; et al. Self-extinguishing Janus separator with high safety for flexible lithium-sulfur batteries. *Sci. China. Mater.* **2022**, *65*, 2169-78. DOI
5. Liu, B.; Fang, R.; Xie, D.; et al. Revisiting scientific issues for industrial applications of lithium-sulfur batteries. *Energy. Environ. Mater.* **2018**, *1*, 196-208. DOI
6. Xue, W.; Shi, Z.; Suo, L.; et al. Intercalation-conversion hybrid cathodes enabling Li-S full-cell architectures with jointly superior gravimetric and volumetric energy densities. *Nat. Energy.* **2019**, *4*, 374-82. DOI
7. Li, H.; Li, Y.; Zhang, L. Designing principles of advanced sulfur cathodes toward practical lithium-sulfur batteries. *SusMat* **2022**, *2*, 34-64. DOI
8. Li, J.; Li, X.; Fan, X.; et al. Holey graphene anchoring of the monodispersed nano-sulfur with covalently-grafted polyaniline for lithium sulfur batteries. *Carbon* **2022**, *188*, 155-65. DOI
9. Li, S.; Fan, Z. Encapsulation methods of sulfur particles for lithium-sulfur batteries: a review. *Energy. Storage. Mater.* **2021**, *34*, 107-27. DOI
10. Feng, L.; Yu, P.; Fu, X.; et al. Regulating polysulfide diffusion and deposition via rational design of core-shell active materials in Li-S batteries. *ACS. Nano.* **2022**, *16*, 7982-92. DOI
11. Zhou, W.; Chen, M.; Zhao, D.; et al. Confined Co_9S_8 nanocrystals into N/S-Co-doped carbon nanofibers as a chainmail-like electrocatalyst for high-performance lithium-sulfur batteries with high sulfur loading. *J. Colloid. Interface. Sci.* **2022**, *625*, 187-96. DOI
12. Xiao, Z.; Li, Z.; Li, P.; Meng, X.; Wang, R. Ultrafine Ti_3C_2 MXene nanodots-interspersed nanosheet for high-energy-density lithium-sulfur batteries. *ACS. Nano.* **2019**, *13*, 3608-17. DOI
13. Chu, R.; Nguyen, T. T.; Bai, Y.; Kim, N. H.; Lee, J. H. Uniformly controlled treble boundary using enriched adsorption sites and accelerated catalyst cathode for robust lithium-sulfur batteries. *Adv. Energy. Mater.* **2022**, *12*, 2102805. DOI
14. Yuan, S.; Xia, M.; Liu, Z.; et al. Dual synergistic effects between Co and Mo_2C in Co/Mo_2C heterostructure for electrocatalytic overall water splitting. *Chem. Eng. J.* **2022**, *430*, 132697. DOI
15. Wang, J.; Yang, J.; Xie, J.; Xu, N. A Novel conductive polymer-sulfur composite cathode material for rechargeable lithium batteries. *Adv. Mater.* **2002**, *14*, 963-5. DOI
16. Wei, S.; Ma, L.; Hendrickson, K. E.; Tu, Z.; Archer, L. A. Metal-sulfur battery cathodes based on PAN-sulfur composites. *J. Am. Chem. Soc.* **2015**, *137*, 12143-52. DOI
17. Zhao, X.; Wang, C.; Li, Z.; Hu, X.; Abdul Razzaq, A.; Deng, Z. Sulfurized polyacrylonitrile for high-performance lithium sulfur batteries: advances and prospects. *J. Mater. Chem. A.* **2021**, *9*, 19282-97. DOI

18. Xie, J.; Chen, J.; Guo, L.; et al. Deciphering the sulfur-involved bonding interactions in sulfurized polyacrylonitrile: the formation thermodynamics and the roles in electrochemical characteristics. *ACS. Nano.* **2025**, *19*, 3931-43. DOI
19. Liu, J.; Wang, M.; Xu, N.; Qian, T.; Yan, C. Progress and perspective of organosulfur polymers as cathode materials for advanced lithium-sulfur batteries. *Energy. Storage. Mater.* **2018**, *15*, 53-64. DOI
20. Chen, W. J.; Li, B. Q.; Zhao, C. X.; et al. Electrolyte regulation towards stable lithium-metal anodes in lithium-sulfur batteries with sulfurized polyacrylonitrile cathodes. *Angew. Chem. Int. Ed.* **2020**, *59*, 10732-45. DOI
21. Doan, T. N. L.; Ghaznavi, M.; Zhao, Y.; et al. Binding mechanism of sulfur and dehydrogenated polyacrylonitrile in sulfur/polymer composite cathode. *J. Power. Sources.* **2013**, *241*, 61-9. DOI
22. Zhang, Y.; Zhao, Y.; Yermukhambetova, A.; Bakenov, Z.; Chen, P. Ternary sulfur/polyacrylonitrile/$Mg_{0.6}Ni_{0.4}O$ composite cathodes for high performance lithium/sulfur batteries. *J. Mater. Chem. A.* **2013**, *1*, 295-301. DOI
23. Fang, L.; Xu, W.; Lyu, X.; et al. Suppressing the shuttle effects with FeCo/SPAN cathodes and high-concentration electrolytes for high-performance lithium-sulfur Batteries. *ACS. Appl. Energy. Mater.* **2023**, *6*, 795-801. DOI
24. He, R.; Li, Y.; Wei, S.; et al. Construction of high-performance sulfurized poly(acrylonitrile) cathodes for lithium-sulfur batteries via catalytic and conductive regulation. *J. Alloys. Compd.* **2022**, *919*, 165838. DOI
25. Wu, S.; Wang, W.; Shan, J.; et al. Conductive 1T-VS_2-MXene heterostructured bidirectional electrocatalyst enabling compact Li-S batteries with high volumetric and areal capacity. *Energy. Storage. Mater.* **2022**, *49*, 153-63. DOI
26. Wang, N.; Chen, B.; Qin, K.; et al. Octopus-inspired design of apical NiS_2 nanoparticles supported on hierarchical carbon composites as an efficient host for lithium sulfur batteries with high sulfur loading. *ACS. Appl. Mater. Interfaces.* **2020**, *12*, 17528-37. DOI
27. Li, Z.; Sami, I.; Yang, J.; Li, J.; Kumar, R. V.; Chhowalla, M. Lithiated metallic molybdenum disulfide nanosheets for high-performance lithium-sulfur batteries. *Nat. Energy.* **2023**, *8*, 84-93. DOI
28. Li, D.; Li, Y.; Xu, C.; Zhao, S.; Zhang, Y.; Huo, P. Enhanced polysulfide adsorption and conversion on FeS_2@CNF-modified separator for Li-S batteries. *New. J. Chem.* **2026**, *50*, 2891-5. DOI
29. Li, Y.; He, R.; Liu, H.; et al. Construction of CoS_2 reduction accelerator-modified sulfurized polyacrylonitrile nanofibers as high-performance cathode materials for practical lithium-sulfur batteries. *ACS. Appl. Energy. Mater.* **2023**, *6*, 8466-78. DOI
30. Liu, Y.; Wang, W.; Wang, A.; Jin, Z.; Zhao, H.; Yang, Y. A polysulfide reduction accelerator - NiS_2-modified sulfurized polyacrylonitrile as a high performance cathode material for lithium-sulfur batteries. *J. Mater. Chem. A.* **2017**, *5*, 22120-4. DOI
31. Yang, W.; Zhao, H.; Chen, L.; et al. Ferrous sulfide-assisted hollow carbon spheres as sulfur host for advanced lithium-sulfur batteries. *Chem. Eng. J.* **2017**, *326*, 1040-7. DOI
32. Lu, X.; Zhang, Q.; Wang, J.; et al. High performance bimetal sulfides for lithium-sulfur batteries. *Chem. Eng. J.* **2019**, *358*, 955-61. DOI
33. Ren, X.; Wang, Q.; Pu, Y.; Sun, Q.; Sun, W.; Lu, L. Synergizing spatial confinement and dual-metal catalysis to boost sulfur kinetics in lithium-sulfur batteries. *Adv. Mater.* **2023**, *35*, e2304120. DOI
34. Dong, H.; Ji, Y.; Wang, L.; et al. Bimetallic coupling strategy modulating electronic construction to accelerate sulfur redox reaction kinetics for high-energy flexible Li-S batteries. *Small* **2024**, *20*, e2406565. DOI
35. Li, N.; Meng, T.; Ma, L.; et al. Curtailing carbon usage with addition of functionalized $NiFe_2O_4$ quantum dots: toward more practical S cathodes for Li-S cells. *NanoMicro. Lett.* **2020**, *12*, 145. DOI
36. Wang, Z.; Song, C.; Shen, H.; Ma, S.; Li, G.; Li, Y. RuO_x quantum dots loaded on graphdiyne for high-performance lithium-sulfur batteries. *Adv. Mater.* **2024**, *36*, e2307786. DOI
37. Xu, Z. L.; Lin, S.; Onofrio, N.; et al. Exceptional catalytic effects of black phosphorus quantum dots in shuttling-free lithium sulfur batteries. *Nat. Commun.* **2018**, *9*, 4164. DOI
38. Kresse, G.; Furthmüller, J. Efficiency of ab-initio total energy calculations for metals and semiconductors using a plane-wave basis set. *Comput. Mater. Sci.* **1996**, *6*, 15-50. DOI
39. Kresse, G.; Furthmüller, J. Efficient iterative schemes for *ab initio* total-energy calculations using a plane-wave basis set. *Phys. Rev. B.* **1996**, *54*, 11169. DOI
40. Kresse, G.; Joubert, D. From ultrasoft pseudopotentials to the projector augmented-wave method. *Phys. Rev. B.* **1999**, *59*, 1758. DOI
41. Perdew, J. P.; Burke, K.; Ernzerhof, M. Generalized gradient approximation made simple [Phys. Rev. Lett. 77, 3865 (1996)]. *Phys. Rev. Lett.* **1997**, *78*, 1396. DOI
42. Babu, B.; Koutavarapu, R.; Shim, J.; Kim, J.; Yoo, K. Improved sunlight-driven photocatalytic abatement of tetracycline and photoelectrocatalytic water oxidation by tin oxide quantum dots anchored on nickel ferrite nanoplates. *J. Electroanal. Chem.* **2021**, *900*, 115699. DOI
43. Miah, M.; Hota, P.; Mondal, T. K.; Chen, R.; Saha, S. K. Mixed metal sulfides ($FeNiS_2$) nanosheets decorated reduced graphene oxide for efficient electrode materials for supercapacitors. *J. Alloys. Compd.* **2023**, *933*, 167648. DOI

44. Liu, H.; Zhang, Y.; Li, Y.; Han, N.; Liu, H.; Zhang, X. Solid-state transformations of active materials in the pores of sulfurized-polyacrylonitrile fiber membranes via nucleophilic reactions for high-loading and free-standing lithium-sulfur battery cathodes. *Adv. Fiber. Mater.* **2024**, *6*, 772-85. DOI
45. Hwang, T. H.; Jung, D. S.; Kim, J. S.; Kim, B. G.; Choi, J. W. One-dimensional carbon-sulfur composite fibers for Na-S rechargeable batteries operating at room temperature. *Nano. Lett.* **2013**, *13*, 4532-8. DOI
46. Wang, X.; Qian, Y.; Wang, L.; et al. Sulfurized polyacrylonitrile cathodes with high compatibility in both ether and carbonate electrolytes for ultrastable lithium-sulfur batteries. *Adv. Funct. Mater.* **2019**, *29*, 1902929. DOI
47. Chen, X.; Peng, L.; Wang, L.; et al. Ether-compatible sulfurized polyacrylonitrile cathode with excellent performance enabled by fast kinetics via selenium doping. *Nat. Commun.* **2019**, *10*, 1021. DOI
48. Lu, J.; Zhang, Y.; Huang, J.; et al. Melamine foam-derived N-doped carbon framework and graphene-supported sulfurized polyacrylonitrile for high performance lithiumsulfur battery cathode. *J. Energy. Storage.* **2025**, *118*, 116330. DOI
49. Abdul Razzaq, A.; Chen, G.; Zhao, X.; et al. Cobalt coordination with pyridines in sulfurized polyacrylonitrile cathodes to form conductive pathways and catalytic M-N_4S sites for accelerated Li-S kinetics. *J. Energy. Chem.* **2021**, *61*, 170-8. DOI
50. Lu, J.; Zhang, Y.; Huang, J.; et al. A free-standing sulfide polyacrylonitrile/reduced graphene oxide film cathode with nacre-like architecture for high-performance lithium-sulfur batteries. *J. Power. Sources.* **2025**, *629*, 235916. DOI
51. Shao, J.; Huang, C.; Zhu, Q.; et al. Flexible CNT-interpenetrating hierarchically porous sulfurized polyacrylonitrile (CIHP-SPAN) electrodes for high-rate lithium-sulfur (Li-S) batteries. *Nanomaterials.* **2024**, *14*, 1155. DOI
52. Hao, C.; Liu, J.; Wang, Q.; et al. High volumetric capacity FeS_2/SPAN composite with promoted kinetics for Li-S battery. *ACS. Nano.* **2025**, *19*, 25385-94. DOI
53. Wang, K.; Guan, Y.; Jin, Z.; Wang, W.; Wang, A. $Te_{0.045}S_{0.955}$PAN composite with high average discharge voltage for Li-S battery. *J. Energy. Chem.* **2019**, *39*, 249-55. DOI
54. Haridas, A. K.; Heo, J.; Li, X.; et al. A flexible and free-standing FeS/sulfurized polyacrylonitrile hybrid anode material for high-rate sodium-ion storage. *Chem. Eng. J.* **2020**, *385*, 123453. DOI
55. Liu, H.; Xu, Q.; Zhang, Y.; Han, N.; Liu, H.; Zhang, X. Multifunctional heterostructure CoS_2/FeS_2 catalysts for enhancing high-performance lithium-sulfurized polyacrylonitrile batteries through intrinsic electric fields. *Chin. Chem. Lett.* **2025**, 111084. DOI
56. Wang, J.; Du, Z.; Lv, G.; et al. Enhancing the backbone regularity of sulfurized polyacrylonitrile for long-life Li-SPAN batteries. *J. Mater. Chem. A.* **2025**, *13*, 21545-54. DOI
57. Gao, G.; Zheng, F.; Pan, F.; Wang, L. W. Theoretical investigation of 2D conductive microporous coordination polymers as Li-S battery cathode with ultrahigh energy density. *Adv. Energy. Mater.* **2018**, *8*, 1801823. DOI
58. Zhao, B.; Ren, Z.; Tan, G.; Li, Z.; Xie, J. Defects on Li_2S@graphene cathode improves the performance of lithium-sulfur battery, A theoretical study. *Acta. Mater.* **2022**, *226*, 117632. DOI